BiFeO3–CoFe2O4–PbTiO3 composites: structural, multiferroic, and optical characteristics

ARTICLE *in* JOURNAL OF MATERIALS SCIENCE · MARCH 2015

Impact Factor: 2.37 · DOI: 10.1007/s10853-014-8769-z

3 AUTHORS, INCLUDING:

Nidhi Adhlakha
Università degli Studi di Torino
12 PUBLICATIONS **33** CITATIONS
SEE PROFILE

Kanhaiya Lal Yadav
Indian Institute of Technology Roorkee
167 PUBLICATIONS **1,606** CITATIONS
SEE PROFILE

J Mater Sci
DOI 10.1007/s10853-014-8769-z

$BiFeO_3$–$CoFe_2O_4$–$PbTiO_3$ composites: structural, multiferroic, and optical characteristics

Nidhi Adhlakha · K. L. Yadav · Ripandeep Singh

Received: 17 July 2014 / Accepted: 3 December 2014

Abstract Three-phase magnetoelectric composites $(1 - x)(0.7BiFeO_3–0.3CoFe_2O_4)–xPbTiO_3$ (or equivalently written as $(1 - x)$(0.7BFO–0.3CFO)–xPT) with x variations 0, 0.30, 0.35, 0.40, 0.45, and 1.0 were synthesized using hybrid processing route. The effects of PT addition on structural, multiferroic, and optical properties have been subsequently investigated. A detailed Rietveld refinement analysis of X-ray diffraction patterns has been performed, which confirms the presence of structural phases of individual constituents in the composites. Field emission scanning electron microscopy images are taken for microstructural analysis and grain size determination. Transmission electron microscopy analysis of 0.3CFO–0.7BFO reveals the average particle size to be lying in the window of 10–15 nm. The temperature-dependent dielectric constant at various frequencies (1, 10, 50, 100, and 500 kHz) has been studied, and the dielectric study reveals the increase of dielectric constant and decrease of average dielectric loss of composites with incorporation of PT content. Room temperature ferromagnetic behavior of composites is confirmed through the observation of magnetization versus magnetic field (M–H) hysteresis loops. The variation of magnetization with temperature indicates the presence of spin glass behavior in composites. Magnetoelectric coupling is evidenced in the composites through the observation of dependence of the dielectric constant on magnetic field, and magnetodielectric response of 2.05 % is observed for 45 mol% addition of PT content. The fractional change of magnetic field-induced dielectric constant can also be expressed as $\Delta\varepsilon_r \sim \gamma M^2$, and the value of γ is found to be $\sim 1.08 \times 10^{-2}$ $(\text{emu/g})^{-2}$ for composite with $x = 0.40$. Fourier transformed infrared spectroscopy of samples is carried out to analyze various bonds formation in the composites.

N. Adhlakha · K. L. Yadav (✉)
Smart Material Research Laboratory, Department of Physics, Indian Institute of Technology Roorkee, Roorkee 247667, India
e-mail: klyadav35@yahoo.com

R. Singh
Solid State Physics Division, Bhabha Atomic Research Centre, Mumbai 400085, India

Introduction

Multiferroics, a class of materials that exhibit ferromagnetic/antiferromagnetic and ferroelectric orderings simultaneously, have attracted a great deal of attention due to their potential applications in quantum electromagnets, microelectronic devices, and spintronic devices [1, 2]. An electric polarization is induced in an applied magnetic field, or a magnetization generated in an external applied magnetic field in such materials. $BiFeO_3$ (BFO) is an outstanding and unique candidate as a single-phase multiferroic material for its high ferroelectric Curie temperature ($T_c \sim 1103$ K) and high G-type antiferromagnetic Neel temperature ($T_N \sim 643$ K). These interesting features permit the multiferroic properties in BFO to be achieved at room temperature. Much attention has been paid toward BFO-based single-phase multiferroic materials due to their potential applications in transducers, sensors, memories, spintronics, and owing to their interesting physics background [3]. Therefore, BFO-based multiferroics have been studied widely in ceramics as well as in thin film-related aspects [4–6].

Despite interesting features mentioned earlier, there are still some problems in bulk BFO like low resistivity, and the observation of net magnetization in bulk BFO is hindered due to presence of intrinsic spatially modulated, incommensurate cycloidal spin structure. The presence of low resistivity is attributed to the valence fluctuations of Fe

Published online: 10 December 2014

ions and existence of secondary phases. These secondary phases can be suppressed by forming BFO-based solid solutions and by optimizing the fabricating process [7]. In chemically substituted bulks and films or in highly constrained epitaxial films [8, 9], slightly enhanced magnetization can be observed, however, this enhancement is limited as only the spin cycloid can be destroyed or suppressed. But it is not possible to change the intrinsic antiferroelectric nature of BFO-based single-phase multiferroics [10]. For increasing magnetism, the effective way is to introduce a suitable ferrite by forming its nanocomposite with BFO. Cobalt ferrite ($CoFe_2O_4$) is well known among the family of ferrite materials as a hard magnetic material with moderate magnetization (about 80 emu/g) and high coercivity (5400 Oe). It exhibits good magnetostrictive properties, remarkable chemical stability, and mechanical hardness with high Neel temperature (520 °C) [11]. This nanocomposite $(1 - x)BiFeO_3$–$xCoFe_2O_4$ appears to be an interesting system which exhibits high magnetic properties and ME effect. With increase of content of $CoFe_2O_4$ to $x = 0.3$, the nanocomposite 0.7BFO–0.3CFO exhibits the largest coercivity and optimal squareness (M_r/M_s) [12].

In past few years, most of the studies were focused on solid solutions of BFO with ABO_3 compounds such as $PbTiO_3$ [13, 14], $BaTiO_3$ [15, 16], and $SrTiO_3$ [17] in order to overcome the deficiencies of single-phase BFO. Moreover in these materials, the increase of ferroelectric polarization was usually accompanied with destruction of their capability of magnetization [18]. On these lines, in recent studies, three-phase composites such as $0.9(0.7BiFeO_3$–$0.3BaTiO_3)$–$0.1CoFe_2O_4$ [10], $(1 - x)[0.9BiFeO_3$–$0.1DyFeO_3]$–$xPbTiO_3$ [19], $BiFeO_3$–$PrFeO_3$–$PbTiO_3$ [20], and $0.7BiFeO_3$–$0.3BaTiO_3$–$Y_3Fe_5O_{12}$ [21] have been developed, and these could simultaneously exhibit improved ferroelectric and magnetic properties.

In this work, we have made an attempt to solve some of the inherent shortcomings of BFO and to obtain improved multiferroic properties by making complex ceramic composites of $(1 - x)(0.7BiFeO_3$–$0.3CoFe_2O_4)$–$xPbTiO_3$ ($x = 0$, 0.30, 0.35, 0.40, 0.45 and 1.0) and investigated their structural, multiferroic, and optical properties. Apart from these, for studying the structural transitions within, we performed a detailed *Rietveld refinement analysis* of X-ray diffraction patterns.

Experimental

Spinel-perovskite $(1 - x)BiFeO_3$–$xCoFe_2O_4$ ($x = 0.30$) nanocomposite was synthesized through sol gel process. The chemical reagents used in the experiment were of analytical grade. The reagents like bismuth nitrate $Bi(NO_3)_3{\cdot}5H_2O$, ferric nitrate $Fe(NO_3)_3{\cdot}9H_2O$, cobalt nitrate $(Co(NO_3)_2{\cdot}6H_2O$, ethylene glycol, and citric acid were used as starting materials. The appropriate molar proportions of metal nitrates were fixed at Bi:Fe:Co in the ratio of 7:13:3. In distilled water, an aqueous solution of citric acid was prepared. Bismuth nitrate, ferric nitrate, and cobalt nitrate were added in turn with constant stirring at 60–70 °C to obtain a homogeneous solution and to avoid precipitation. After mixing of the salts to their total dissolution, ethylene glycol was subsequently added into the solution with a proportion (in mass) of citric acid/ethylene glycol ratio of 70:30. The solution was then turned into xerogel that started to swell and filled the beaker generating a foamy precursor, which consisted of very light flakes of nanosize. The resulting gel obtained was then dried overnight at 100 °C in a hot air oven to remove the excess water, and the powder obtained after drying was calcined at 600 °C for 2 h. The obtained calcined powder was then leached in diluted HNO_3 to obtain single phase of nanoceramics.

$PbTiO_3$ was prepared through solid state reaction method. The stoichiometric amounts of analytical grade powders of PbO and TiO_2 were weighed and mixed thoroughly in an acetone media using agate mortar for 5–6 h. The well-mixed powder was then dried and presintered in a closed alumina crucible at 1000 °C for 2 h in an air atmosphere. In order to get uniform particle size, the calcined powder was crushed and grounded. This fine powder was then used for the synthesis of magnetoelectric composites.

The composites having specific formula $(1 - x)(0.7BiFeO_3$–$0.3CoFe_2O_4)$–$xPbTiO_3$ where $x = 0$, 0.30, 0.35, 0.40, 0.45, and 1.0 were prepared by mixing 0.7BFO–0.3CFO and PT in an acetone medium with the respective proportion as mentioned. These mixed powders were then pressed into disks of 8 mm diameter and 1–2 mm thickness using a steel die and hydraulic press with uniaxial pressure of about 6×10^7 kg/m^2. The obtained disks were finally sintered at 950 °C for 2 h.

The phase identification of sintered pellets was carried out using X-ray diffractometer (Bruker D8 Advance) at a scanning rate of 1°/min. at room temperature using Cu$K\alpha$ radiation ($\lambda = 1.5418$ Å). The X-ray diffraction patterns corresponding to the (0.7BFO–0.3CFO)/PT composites were analyzed using a program FULLPROF by utilizing Rietveld refinement technique. The distribution of grains on the surface of sintered pellets was analyzed by taking field emission scanning electron microscopy (FESEM) images with the help of FEI Quanta 200FEG electron microscope operating at an accelerating voltage of 20 kV. Moreover, using linear intercept method the grain size was calculated from the micrographs of FESEM. Transmission electron microscopy (TEM) image was taken using FEI, Technai G^2

TEM setup. For taking electrical measurements, the flat surfaces of pellets were polished with high purity silver paste and then dried at 150 °C for 2 h. The measurement of dielectric constant (ε) and dielectric loss (tan δ) were carried out using an automated HIOKI 3532-50 Hi-Tester LCR meter connected to desktop computer, capacitance measuring assembly, in the temperature range of 30–500 °C at different frequencies (1 kHz, 10 kHz, 50 kHz, 100 kHz, 500 kHz and 1 MHz). The magnetic measurements on composites were taken using Superconducting Quantum Interference Device (SQUID) at room temperature (300 K) and 5 K under an applied magnetic field of 500 Oe. Magnetocapacitance study was performed using a Wayne Kerr 6500 high frequency LCR meter along with a magnet up to 8 kOe having an accuracy of 10 Oe (provided by Marine India Electr. Pvt. Ltd.). The Fourier transform infrared spectra (FTIR) were recorded for the dried samples embedded in KBR matrix using FTIR spectrophotometer (NEXUS Thermo Nicolet IR-spectrometer) in the range of 2000–400 cm^{-1}.

Results and discussion

Structural and microstructural characterizations

Figure 1a–f shows the X-ray diffraction patterns along with the Rietveld refined data of $(1 - x)(0.7BiFeO_3–0.3CoFe_2O_4)–xPbTiO_3$ ($x = 0$, 0.30, 0.35, 0.40, 0.45, and 1.0) composites. The Rietveld refinement of the XRD patterns of composites consisting of BFO, CFO, and PT phases was carried out using the space groups *R*3*c*, *Fd*-3*m*, and *P*4*mm*, respectively. The existence of individual phases corresponding to CFO, BFO, and PT without any signature of intermediate phases was detected in all the compositions which clearly revealed their chemical compatibility with no chemical reaction.

The Rietveld refinement technique is a well-established method to obtain detailed structural parameters from powder diffraction technique. In Rietveld refinement method, using the least square procedure, the Bragg intensities are compared with those calculated from a possible structural model. Both the structural (atomic positions, occupancies, and lattice constants) and microstructural (lattice strain) parameters are refined simultaneously with Rietveld analysis. Figure 1a–f shows the observed, calculated, and the difference patterns obtained using Rietveld refinement. It has been found that there is a good agreement in observed and calculated XRD patterns which is further confirmed by observing the difference pattern.

This clearly implies that all observed peak positions and peak intensities could be reproduced well using aforementioned structural models for the composites. The experimental data in Fig. 1a–f is shown as closed circles (red) and the solid lines (black) depict the calculated

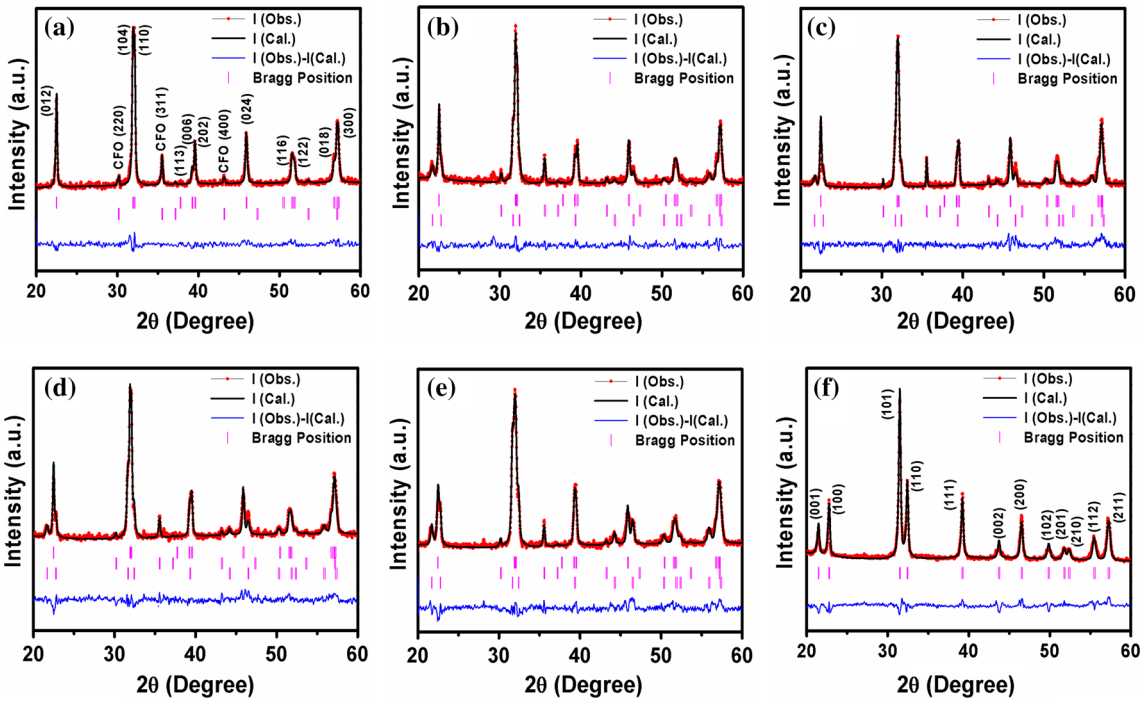

Fig. 1 X-ray diffraction patterns and Rietveld refined results for $(1 - x)(0.7BiFeO_3–0.3CoFe_2O_4)–xPbTiO_3$ **a** $x = 0$, **b** $x = 0.30$, **c** $x = 0.35$, **d** $x = 0.40$, **e** $x = 0.45$, and **f** $x = 1.0$ composites, along with observed (Obs.), calculated (cal.) and difference patterns

intensities. The difference between measured and calculated intensities is represented by bottom line (blue). The allowed Bragg positions for the space groups *R*3*c*, *Fd*-3*m* and *P*4*mm* are shown as vertical lines (pink). The parameters such as R-factors (R_F = crystallographic factor, R_B = Bragg factor) and the 'goodness of fit index' (χ^2) were computed to assess the fitting quality and the reliability of experimental data. The best fit of the experimental diffraction data is achieved when these parameters reached their minimum value and hence the corresponding crystal structure is considered as satisfactory [22]. The detailed structural parameters and microstructural parameter (crystallite size) attained from the refinement along with the profile *R*-factors for composites with $x = 0$, 0.30 and 0.35 are listed in Table 1 and for composites with $x = 0.40$, 0.45 and 1.0 are listed in Table 2. The refined lattice parameters (shown in Table 1) of individual phases in the composites are observed to be almost equal to the pure 0.7BFO–0.3CFO phase and pure PT phase, which clearly signifies that there is no structural change of the individual phases during formation of composites. The refined positional coordinates for composites with $x = 0$, 0.30 and 0.35 are listed in Table 3, and for composites with $x = 0.40$, 0.45 and 1.0 are listed in Table 4. The atomic coordinates and the initial model for BFO, CFO, and PT are taken from literature [23–25].

Figure 2a–c shows the schematic plots of unit cells of $BiFeO_3$, $CoFe_2O_4$, and $PbTiO_3$ in hexagonal setting of space group *R*3*c*, cubic spinel structure with space group *Fd*-3*m*, and tetragonal symmetry with space group *P*4*mm*, respectively, for $(1-x)(0.7BiFeO_3–0.3CoFe_2O_4)–xPbTiO_3$ composite with $x = 0.30$. These are determined from our data in which all the structures were drawn using cell parameters and positional parameters obtained from the refinement.

Figure 3a–f displays the FESEM micrographs of $(1-x)(0.3CoFe_2O_4–0.7BiFeO_3)–xPbTiO_3$ with $x = 0$, 0.30, 0.35, 0.40, 0.45, and 1.0 ceramics consisting of randomly oriented and non-uniform (both in shape and size) grains. The grains

Table 1 Rietveld refined XRD parameters and grain size of $(1-x)(0.3CoFe_2O_4–0.7BiFeO_3)–xPbTiO_3$ composite ceramics with $x = 0$, 0.30, and 0.35

Compositions	$x = 0$	$x = 0.30$	$x = 0.35$
Space group	*R*3*c*	*R*3*c*	*R*3*c*
	Fd-3*m*	*Fd*-3*m*	*Fd*-3*m*
		*P*4*mm*	*P*4*mm*
Lattice parameters			
BFO phase			
a (Å)	5.572	5.573	5.583
c (Å)	13.781	13.780	13.782
Volume (Å^3)	370.560	370.662	371.977
CFO phase			
a (Å)	8.382	8.379	8.377
Volume (Å^3)	588.793	588.236	587.760
PT phase			
a (Å)	–	3.908	3.908
c (Å)		4.101	4.094
Volume (Å^3)		62.642	62.495
R_{exp}	9.23	13.8	14.1
R_{Bragg}			
BFO	11.3	6.70	12.3
CFO	18.2	24.9	32.4
PT	–	16.9	18.6
R_f			
BFO	8.18	5.59	7.88
CFO	16.1	14.2	23.5
PT	–	13.3	16.3
χ^2	1.13	1.15	1.28
Grain size (nm)	1393	1162	826
Bulk density (g/cm^3)	5.27	6.14	7.28

Table 2 Rietveld refined XRD parameters and grain size of $(1-x)(0.3CoFe_2O_4–0.7BiFeO_3)–xPbTiO_3$ composite ceramics with $x = 0.40$, 0.45, and 1.0

Compositions	$x = 0.40$	$x = 0.45$	$x = 1.0$
Space group	*R*3*c*	*R*3*c*	*R*3*c*
	Fd-3*m*	*Fd*-3*m*	*Fd*-3*m*
	*P*4*mm*	*P*4*mm*	*P*4*mm*
Lattice parameters			
BFO phase			
a (Å)	5.578	5.580	–
c (Å)	13.776	13.771	
Volume (Å^3)	371.253	371.283	
CFO phase (Å)			
a (Å)	8.371	8.368	–
Volume (Å^3)	586.549	585.916	
PT phase (Å)			
a (Å)	3.906	3.906	3.905
c (Å)	4.098	4.093	4.139
Volume (Å^3)	62.529	62.435	63.128
R_{exp}	13.3	13.2	16.7
R_{Bragg}			
BFO	11.5	8.36	–
CFO	21.9	23.5	–
PT	14.7	12.3	10.7
R_f			
BFO	7.09	5.53	–
CFO	11.9	13.9	–
PT	10.7	8.82	7.00
χ^2	1.27	1.33	1.57
Grain size (nm)	717	671	2045
Bulk density (g/cm^3)	7.50	8.35	7.40

Table 3 Refined structural parameters of $(1 - x)(0.7BiFeO_3–0.3CoFe_2O_4)–xPbTiO_3$ composites with $x = 0$, 0.30, and 0.35

Compositions		$x = 0$			$x = 0.30$			$x = 0.35$		
Positional coordinates		*X*	*Y*	*Z*	*X*	*Y*	*Z*	*x*	*y*	*z*
BFO phase	Bi	0	0	0.3073	0	0	0.3000	0	0	0.3179
	Fe	0	0	0.0319	0	0	0	0	0	0.0515
	O	0.8622	0.6468	0.5178	0.8820	0.6820	0.5000	0.8374	0.6501	0.5154
CFO phase	O	0.2668	0.2668	0.2668	0.2700	0.2700	0.2700	0.2562	0.2562	0.2562
	FeT[a]	0.1250	0.1250	0.1250	0.1250	0.1250	0.1250	0.1250	0.1250	0.1250
	FeO[b]	0.5000	0.5000	0.5000	0.5000	0.5000	0.5000	0.5000	0.5000	0.5000
	CoO[b]	0.5000	0.5000	0.5000	0.5000	0.5000	0.5000	0.5000	0.5000	0.5000
PT phase	Pb	–	–	–	0	0	0	0	0	0
	Ti	–	–	–	0.5000	0.5000	0.4360	0.5000	0.5000	0.4478
	O1	–	–	–	0.5000	0.5000	−0.030	0.5000	0.5000	0.0998
	O2	–	–	–	0.5000	0	0.6900	0.5000	0	0.6088

[a] Symbol T denotes the tetrahedral sites

[b] Symbol O denotes the octahedral sites

of 0.3CFO–0.7BFO and PT are found to be closely packed in the composites. The mixed microstructures of composites with different grain size and few pores are clearly revealed from the micrographs. The probability of grain growth of one of the phase is higher as compared to the other, therefore they grow at the expense of the smaller ones [26]. The average grain size of pure PT (Table 2) prepared through solid-state reaction method is higher as compared to that of 0.3CFO–0.7BFO (Table 1) prepared by sol–gel process. The microstructures become denser with increase of PT content. The bulk density of the sintered ceramic composites was measured using Archimedes method, and the density data are given in Table 1 for composites with $x = 0$, 0.30 and 0.35, and in Table 2 for composites with $x = 0.40$, 0.45 and 1.0. It shows that the PT addition leads to densification of ceramic composites. The larger grain size of PT (Table 2) is effective in reducing the leakage of electric charges which occurs due to a chain formation of the ferrite phase particles, so the dielectric and ferroelectric properties of composites are improved with addition of PT content [27]. The addition of PT content leads to inhibition of grain growth due to reduction of oxygen ion vacancies with its addition.

Figure 4a shows the representative Transmission electron micrograph (TEM) of calcined $0.7BiFeO_3–0.3CoFe_2O_4$ nanoparticles and Fig. 4b shows the corresponding selected area electron diffraction (SAED) pattern. The TEM image reveals the agglomeration of the particles having approximately spherical morphology. The polycrystalline nature of the nanoparticles is manifested from the sharp circular distinct ring patterns corresponding to the different lattice planes observed in the SAED pattern. The average particle size calculated using TEM micrograph, which is composed of several crystallites, is found to lie between 10 and 15 nm, approximately. The average grain size of the composites calculated using linear intercept method from FESEM images is found to be 1393, 1162, 826, 717, 671, and 2045 nm for $(1 - x)(0.7BiFeO_3–0.3CoFe_2O_4)–xPbTiO_3$ composites with $x = 0$, 0.30, 0.35, 0.40, 0.45, and 1.0, respectively. FESEM is used to calculate the size of grain which is agglomeration of particles.

The XRD, FESEM, and TEM probe the structural aspects of problem differently due to difference in their interaction with matter. Whereas XRD being scattering probe gives the statistical average information about the system, FESEM and TEM are local probes which gives idea about the part of system one is looking at. X-rays ($\lambda = 1.5402$ Å) with energy around 8.06 keV are used in X-ray diffractometer to take the pattern of material. In FESEM, the energy of the incident electron beam which is used to locate particle lies in the range of 1–50 keV, and the study of electrons scattered or reflected in a backward direction and emitted secondary electrons is performed. However, in TEM, the energy of electrons used is usually between 40 and 200 keV and information obtained is from the electrons which are transmitted through the specimen.

The particle size determined by XRD analysis is average crystallite size which is different from particle size observed from FESEM and TEM. The crystallite size which is obtained from the XRD is equal to the average size of the domains which scatter X-rays coherently. Hence the crystallite size which is obtained from the XRD is always less than the particle size obtained by FESEM and TEM.

Dielectric measurements

Figure 5a–f shows the temperature dependence of the dielectric constant (ε) at various frequencies (1, 10, 50, 100, and 500 kHz) and the inset shows the corresponding variation of loss tangent (tan δ) with temperature. It is observed that the value of dielectric constant increases with increase of temperature up to a certain transition

Table 4 Refined structural parameters of $(1 - x)(0.7BiFeO_3–0.3CoFe_2O_4)–xPbTiO_3$ composites with $x = 0.40$, 0.45, and 1.0

Compositions		$x = 0.40$			$x = 0.45$			$x = 1.0$		
Positional coordinates		***x***	*y*	*z*	***x***	*y*	*z*	***x***	*y*	*z*
BFO phase	Bi	0	0	0.3070	0	0	0.3185	–	–	–
	Fe	0	0	0.0400	0	0	0.0536	–	–	–
	O	0.8831	0.6737	0.5067	0.8717	0.6694	0.5216	–	–	–
CFO phase	O	0.2585	0.2585	0.2585	0.2710	0.2710	0.2710	–	–	–
	FeT[a]	0.1250	0.1250	0.1250	0.1250	0.1250	0.1250	–	–	–
	FeO[b]	0.5000	0.5000	0.5000	0.5000	0.5000	0.5000	–	–	–
	CoO[b]	0.5000	0.5000	0.5000	0.5000	0.5000	0.5000	–	–	–
PT phase	Pb	0	0	0	0	0	0	0	0	0
	Ti	0.5000	0.5000	0.4405	0.5000	0.5000	0.4523	0.5000	0.5000	0.4628
	O1	0.5000	0.5000	0.0739	0.5000	0.5000	0.0191	0.5000	0.5000	0.1195
	O2	0.5000	0	0.5797	0.500	0	0.5814	0.5000	0	0.5932

[a] Symbol T denotes the tetrahedral sites

[b] Symbol O denotes the octahedral sites

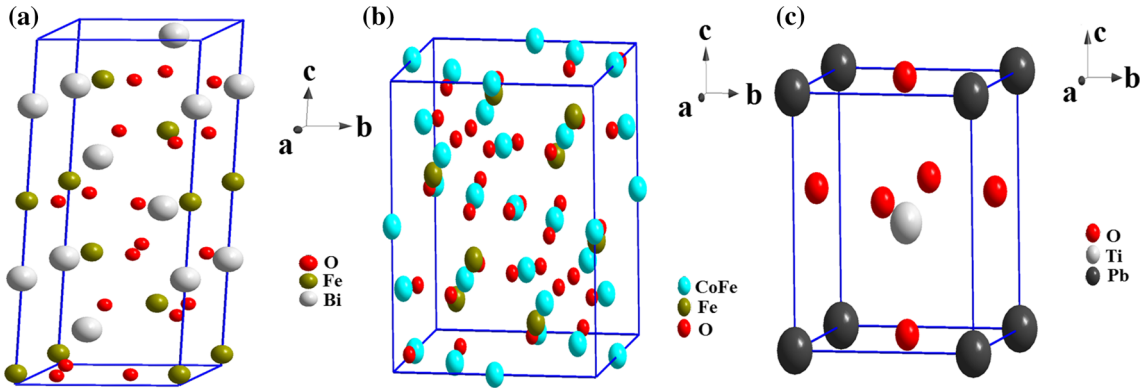

Fig. 2 Schematic presentation of unit cells of **a** $BiFeO_3$ in hexagonal setting of space group *R*3*c*, **b** $CoFe_2O_4$ in cubic spinel structure with space group *Fd*-3*m*, and **c** $PbTiO_3$ having tetragonal symmetry with space group *P*4*mm*

temperature beyond which it decreases. The increase of dielectric constant with increase of temperature is due to hopping of charge carriers which is a thermally activated process. It is clear from Fig. 5a that 0.7BFO–0.3CFO exhibits diffuse phase transition (DPT) with broad maxima in the dielectric behavior, and with increase of frequency, the maxima shifts to higher temperature side. The cation disorder due to nanoscaled ordered microregions in complex perovskite is generally responsible for DPT [28].

The relaxor behavior is exhibited by the composites in which there is a shift in the peak of relative permittivity with frequency; however, this behavior is not shown by $PbTiO_3$. The values of transition temperatures for $(1 - x)(0.7BiFeO_3–0.3CoFe_2O_4)–xPbTiO_3$ composites with $x = 0$, 0.30, 0.35, 0.40, 0.45, and 1.0 at 1 kHz frequency are 270, 385, 390, 425, 485, and 460 °C, respectively. The peaks become narrower and shift to the higher temperature side with increase of PT content. The dielectric constant is higher at low frequencies, because of the fact that the contribution of dipolar and interfacial polarizations is significant at these frequencies; however, at higher frequencies the electronic polarization becomes dominant. Therefore, the rate of increase of dielectric constant at 1 kHz frequency is higher as compared to other frequencies. The variation of loss factor with temperature (inset of Fig. 5a–f) indicates that at higher temperatures, the loss factor increases rapidly which clearly indicates the space charge conduction. The transport of defects such as oxygen vacancies to dielectric-electrode interface is responsible for space charge conduction [29, 30]. Moreover, an inherent problem of non-stoichiometric oxygen deficiency is associated with BFO due to which in the whole temperature range there is contribution of space charge polarization associated with the oxygen vacancies. This effect becomes striking at higher temperatures because of thermally activated process which leads to shoot up of dielectric loss to a high value. It has also been found that at higher frequency (500 kHz), the dielectric loss is significantly smaller as compared to lower frequencies. The dielectric constant of PT is higher and dielectric loss is lower (Fig. 5f) as compared to 0.7BFO–0.3CFO (Fig. 5a). With

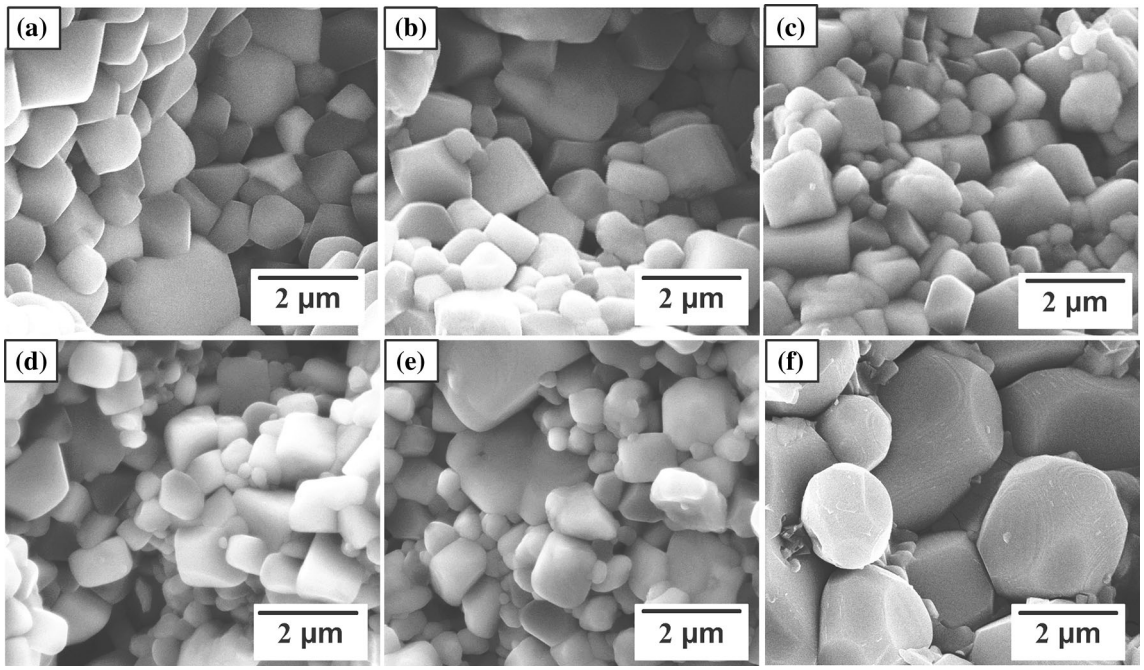

Fig. 3 FESEM micrographs of fractured surfaces of $(1 - x)(0.3CoFe_2O_4–0.7BiFeO_3)–xPbTiO_3$ composites **a** $x = 0$, **b** $x = 0.30$, **c** $x = 0.35$, **d** $x = 0.40$, **e** $x = 0.45$, and **f** $x = 1.0$

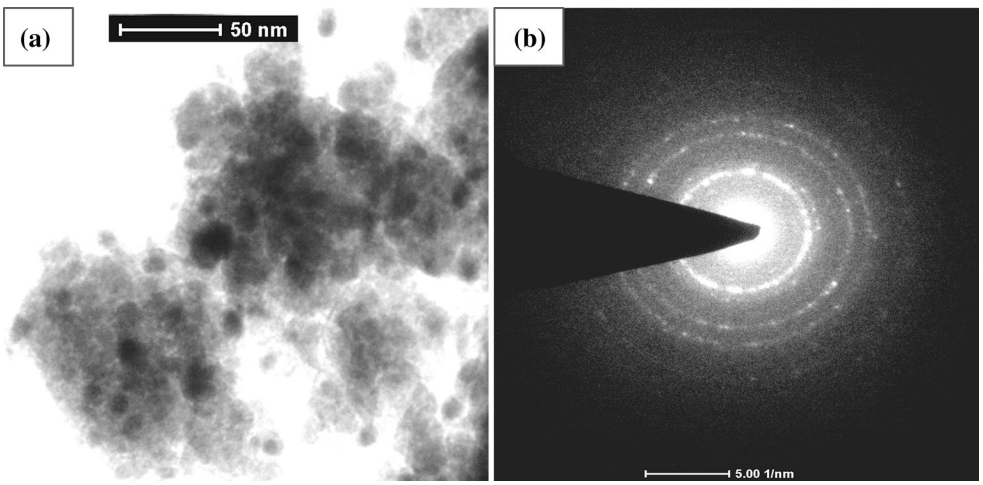

Fig. 4 **a** TEM image of $0.7BiFeO_3–0.3CoFe_2O_4$ nanoparticles and the corresponding. **b** Selected area electron diffraction pattern

incorporation of PT content, the value of dielectric constant is increased for the composites, and also the reduction in dielectric loss has been observed. The increase of dielectric constant and decrease of average dielectric loss with addition of PT content is believed to be caused by improved densification (given in Tables 1, 2) in the ceramic composites with addition of PT [31, 32].

Magnetic characterization

Figure 6a–b shows the magnetization versus magnetic field (M–H) loops of $(1 - x)(0.7BiFeO_3–0.3CoFe_2O_4)–xPbTiO_3$ ($x = 0$, 0.30, 0.35, 0.40 and 0.45) composites obtained by applying field up to 7 T at 300 and 5 K, respectively. The inset of Fig. 6a shows the enlarged M–H curve around the origin for composite with $x = 0$ in order to show the value of coercivity. The ceramics exhibit hysteresis loops typical of ferromagnetic behavior at room temperature (300 K) and at low temperature (5 K), which indicates the presence of an ordered magnetic structure that can exist in spinel-perovskite mixed system. The $CoFe_2O_4$ content mainly contributes to the ferromagnetic behavior of the composites, as $BiFeO_3$ exhibits antiferromagnetic nature, preferably G-type magnetic structure and it does not have any

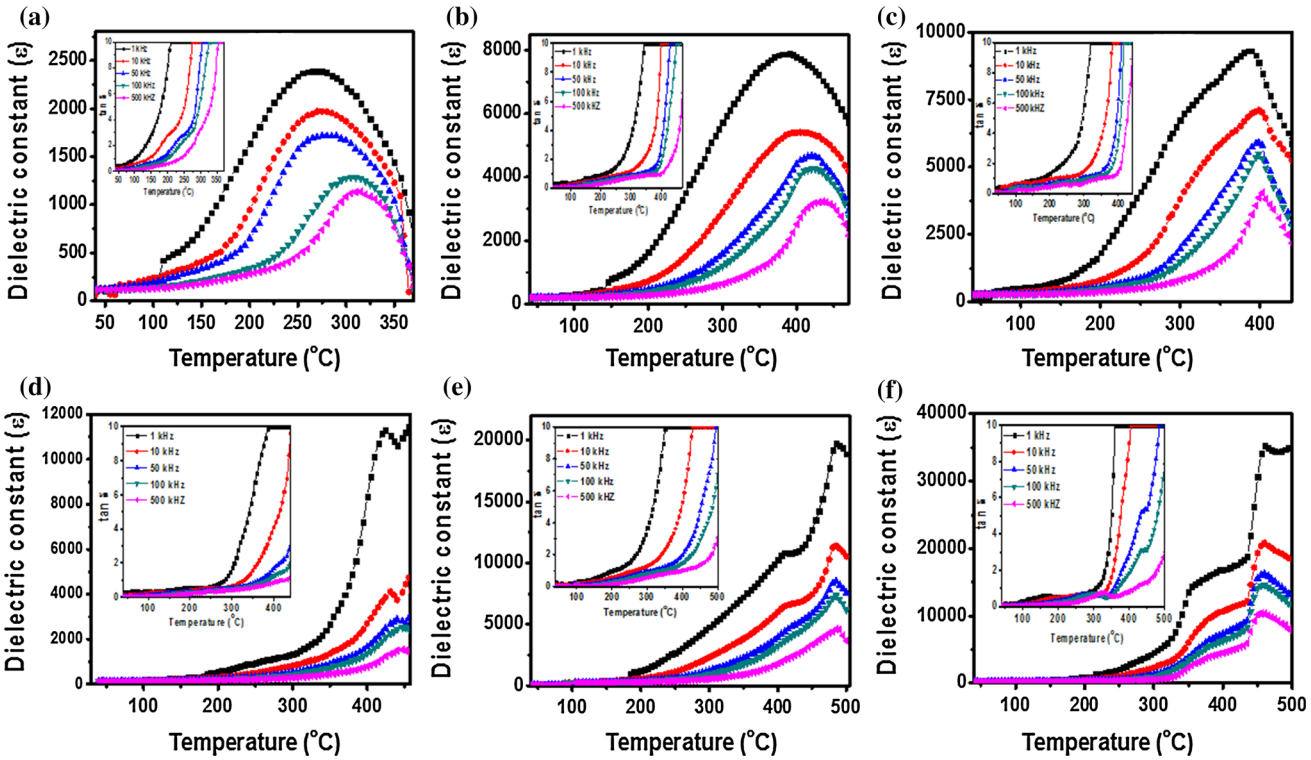

Fig. 5 Dielectric constant as a function of temperature for $(1 - x)(0.7BiFeO_3–0.3CoFe_2O_4)–xPbTiO_3$ composites **a** $x = 0$, **b** $x = 0.30$, **c** $x = 0.35$, **d** $x = 0.40$, **e** $x = 0.45$, and **f** $x = 1.0$. The *inset* shows the temperature dependence of dielectric loss for the corresponding compositions

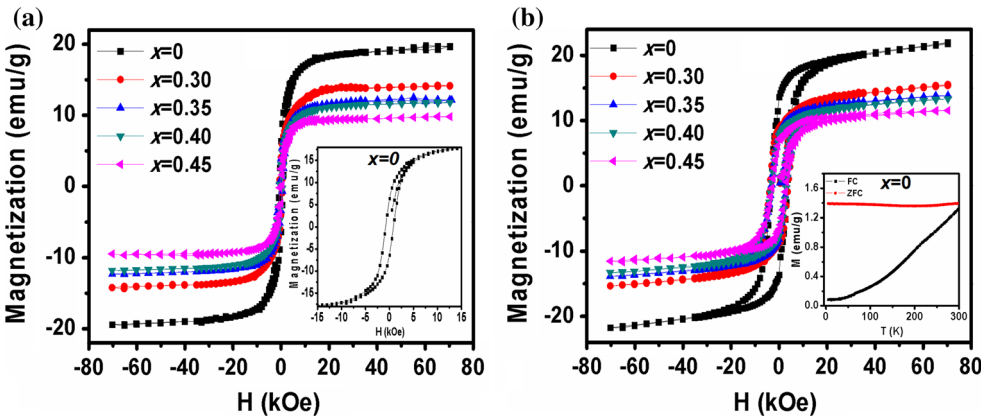

Fig. 6 Magnetization versus magnetic field (M–H) characteristics of $(1 - x)(0.7BiFeO_3–0.3CoFe_2O_4)–xPbTiO_3$ composites at temperatures **a** 300 K and **b** 5 K. The *inset* of **a** shows the magnified part of the hysteresis loop of composite with $x = 0$ in the low-field range and the *inset* of **b** shows the temperature dependence of FC and ZFC magnetizations of composite with $x = 0$

macroscopic magnetization at room temperature [33]. The antiferromagnetism of BFO is turned into ferromagnetism with addition of 30 mol% CFO which may be due to the suppression of spiral spin modulation. The magnetic parameters such as saturation magnetization ($2M_s$), remnant magnetization ($2M_r$), coercive field ($2H_c$), and Bohr magneton (μ_B) were calculated from the hysteresis loops at 300 and 5 K, respectively, and are shown in Table 5.

The magnetic moment in Bohr magneton (μ_B) was calculated using the following relation (1):

$$\mu_B = \frac{M\sigma'_s}{5585}, \tag{1}$$

where σ'_s is the magnetization per gram mol of the sample, M is the molecular weight, and 5585 is the magnetic factor.

The composite 0.7BFO–0.3CFO exhibits high value of saturation magnetization and coercive field (shown in Table 5). This may be due to the presence of magneto-elastic interaction between two phases of the nanocomposite. This interaction arises due to magnetostriction of CFO phase which is attributed to domain wall motion and

domain rotation, and is involved in ME effect [12]. The values of saturation magnetization ($2M_s$), remnant magnetization ($2M_r$), and Bohr magneton (μ_B) are found to be reduced with increase of PT content. In case of ferrite-ferroelectric composites, the ferrite grains contribute to net magnetization and the ferroelectric component acts as pores among the grains in the presence of an applied magnetic field. With increase of pore concentration, the magnetic parameters are found to decrease as these pores break the magnetic circuit [34]. There is an enhancement of magnetic parameters with lowering of temperature from 300 to 5 K due to ordering of magnetization at low temperatures (5 K) (shown in Table 5). The large value of coercivity at low temperature inferred that CFO exhibits single magnetic domain along with large crystal magnetic anisotropy at low temperature [35]. However, at low temperatures (5 K), the *M–H* loops are not saturated even at 75 kOe. Figure 6b indicates that there may be two contributions which are responsible for such a behavior at low temperatures. The hysteretic behavior of the composites is mainly due to ferromagnetic contribution, and the linear nature of the *M–H* loop at higher magnetic field is due to contribution of paramagnetic host which indicates that the magnetically ordered clusters exist in a paramagnetic host [36].

In order to further illustrate the magnetic ordering in the composites, the temperature dependence of zero-field-cooled (ZFC) magnetization and field-cooled (FC) magnetization curves was measured in the temperature range of 5–300 K. The inset of Fig. 6b shows the temperature dependence of magnetization for $(1-x)(0.7BiFeO_3–0.3CoFe_2O_4)–xPbTiO_3$ composite with $x = 0$. The samples were cooled to a desired temperature in ZFC mode, and a magnetic field of 500 Oe was applied to get measurement in FC mode. The large discrepancy between the ZFC and FC magnetic curves at low temperatures inferred the presence of strong irreversibility effect. The separation of ZFC and FC curves occurs at a particular temperature called irreversibility temperature (T_{irr}); this is the temperature where irreversible magnetization M_{irr} ($M_{irr} = M_{FC} - M_{ZFC}$) becomes non-zero, and ZFC and FC branches merge [36]. One of the most probable reasons for an increase of the difference viz. $M_{FC}–M_{ZFC}$ with a decrease of temperature is the presence of spin glass behavior. Similar behavior is observed in other composites with $x = 0.30$, 0.35, 0.40, and 0.45. The system can be modeled in the framework of Neel's theory of fine particles, according to which the strongly coupled cluster of spins together with a weak random field gives rise to an overall spin glass-like behavior [37]. The origin of this spin glass behavior can also be demonstrated in the way that, this behavior arises when the sign of neighboring coupling spins appears in a random manner and further their combination with mixed interactions induces frustration in the system [38].

Magnetodielectric studies

The magnetic field (H) dependence of dielectric constant ($\Delta\varepsilon_r$) was measured at 1 kHz frequency at room temperature to study the magnetoelectric coupling between electric and magnetic dipoles. This variation of dielectric constant with an applied magnetic field is known as magnetocapacitance (MC) effect or magnetodielectric (MD) effect, which is defined as Eq. (2):

$$\mathrm{MC} = \frac{\varepsilon(H) - \varepsilon(0)}{\varepsilon(0)} \times 100, \tag{2}$$

where $\varepsilon(H)$ and $\varepsilon(0)$ represent the dielectric constant in the presence and absence of an applied magnetic field, respectively. The variation of dielectric constant with an applied magnetic field (varied up to 85 kOe) for $(1-x)(0.7BiFeO_3–0.3CoFe_2O_4)–xPbTiO_3$ composites with x variations 0, 0.30, 0.35, 0.40, and 0.45 at 1 kHz frequency and at room temperature is shown in Fig. 7a.

Under an applied magnetic field, the absolute value of MC first increases and thereafter remains almost constant. At $H = 6$ kOe, the values of MC for composites with $x = 0$, 0.30, 0.35, 0.40, and 0.45 are found to be 0.31, 0.51, 0.74, 1.15, and 2.05 %, respectively. The value of magnetocapacitance is found to increase with increase of PT content and its highest value is found to be 2.05 % for 45 mol% addition of PT. The observed value of magnetocapacitance is higher as compared to $BiFeO_3/CoFe_2O_4$ bilayered films [39] reported earlier.

Table 5 Magnetic parameters of $(1-x)(0.7BiFeO_3–0.3CoFe_2O_4)–xPbTiO_3$ composites observed at 300 and 5 K

Composition (x)	$2M_r$ (emu/g)		$2M_s$ (emu/g)		$2H_c$ (kOe)		Magnetic moment (μ_B)	
	300 K	5 K	300 K	5 K	300 K	5 K	300 K	5 K
0.00	12.762	27.269	39.137	43.776	1.631	6.703	1.014	1.134
0.30	8.086	17.432	28.284	30.868	1.236	7.380	0.862	0.941
0.35	7.299	16.397	24.436	27.687	1.192	6.022	0.763	0.865
0.40	6.041	15.445	23.586	26.614	1.089	5.961	0.755	0.852
0.45	4.892	13.766	19.463	23.082	0.961	5.668	0.638	0.756

The magnetodielectric behavior may be originated due to several possible reasons such as magnetoresistance effect, magnetostriction effect, or magnetoelectric coupling. In order to check the presence of magnetoresistance, the change of resistance with an applied magnetic field was measured, and it has been found the change in the resistance with magnetic field is not very large ($\sim$0.038 %). Hence magnetocapacitance is not ascribed to the magnetoresistance. Palkar et al. [40] have envisaged that such a behavior of magnetocapacitance indicates the occurrence of magnetoelectric (ME) coupling in the ceramics.

The Gibbs free energy $G(T, P, M)$ of a multiferroic on the basis of Landau theory can be written as a Taylor series expansion of the order parameters i.e., polarization (P) and magnetization (M) [41]. The coefficient corresponding to P^2M^2 term in the expansion is the ME coupling parameter. As per Zhou et al. [41], the coefficient corresponding to P^2M^2 term gives the strain transitions between ferroelectric and ferromagnetic phases. This parameter is non-zero when there is ME coupling, and is zero otherwise. Moreover, the thermodynamic potential [42] of a ferroelectromagnet can be written in the form of Eq. (3):

$$\varphi = \varphi_0 + \alpha P^2 + \frac{\beta}{2}P^4 - PE + \alpha' P^2 + \frac{\beta'}{2}M^4 - MH + \gamma P^2 M^2, \quad (3)$$

where $\alpha, \beta, \alpha', \beta'$, and γ are coupling coefficients, and P and M are the order parameters for polarization and magnetization, respectively. The term γP^2M^2, representing the magnetoelectric interaction is always allowed regardless of symmetry. Kimura et al. [42] used this free energy expression to calculate the effect of magnetic ordering on dielectric susceptibility and found that the effect of magnetic ordering on dielectric constant will be proportional to $\Delta\varepsilon_r \sim \gamma M^2$. The sign of $\Delta\varepsilon_r$ can be either positive or negative depending on the sign of magnetoelectric interaction constant γ. We have calculated here the value of γ for 0.6(0.7$BiFeO_3$–0.3$CoFe_2O_4$)–0.4$PbTiO_3$ composite. Figure 7 (b) shows the variation of $\Delta\varepsilon/\varepsilon(0)$ with square of magnetization (M^2) for $(1-x)$(0.7$BiFeO_3$–0.3$CoFe_2O_4$)–$x$$PbTiO_3$ composite with $x = 0.40$ and a linear change has been observed, which means that the aforementioned relation ($\Delta\varepsilon_r \sim \gamma M^2$) is followed by the composite. The observation of linear behavior leads to the conclusion that the magnetocapacitance observed in the system arises from the coupling term γP^2M^2 in thermodynamic potential [42]. The inset of Fig. 7b shows the variation of M^2 with an applied magnetic field up to 8 kOe. The value of γ was calculated using linear fitting and it was found to be $\sim 1.08 \times 10^{-2}$ (emu/g)$^{-2}$ for composite with $x = 0.40$.

FTIR spectral analysis

The Fourier transform infrared spectra (FTIR) of $(1-x)$(0.7$BiFeO_3$–0.3$CoFe_2O_4$)–$x$$PbTiO_3$ ceramics composites with $x = 0$, 0.30, 0.35, 0.40, 0.45, and 1.0 are shown in Fig. 8. This technique is used in order to identify the chemical bands of different phases in chemical compounds. FTIR spectra can offer the information about the redistribution of cations between tetrahedral and octahedral sites in case of ferrites as ferrite structures comprise of two sublattices viz. tetrahedral and octahedral groups.

The vibrational band appearing at 590 cm^{-1} is assigned to metal–oxygen stretching mode of $CoFe_2O_4$ and hence can be assigned to vibrations of Fe–O or Co–O [43]. This band is characteristic absorption band of Co(Fe)–O [44]. The presence of peaks centered around 405 and 590 cm^{-1} are attributed to metal–oxygen bonding peaks of $PbTiO_3$ [45, 46]. The peak centered around 405 cm^{-1} is absent in pure 0.3CFO–0.7BFO, but appears in the composites with addition of PT. With addition of PT in composites the peaks corresponding to PT phase also appear along with the 0.7BFO–0.3CFO phase vibrational bands which clearly depict the successful formation of composites being also clear from XRD pattern [Fig. 1]. The presence of absorption band at around 650 cm^{-1} is ascribed to bending modes

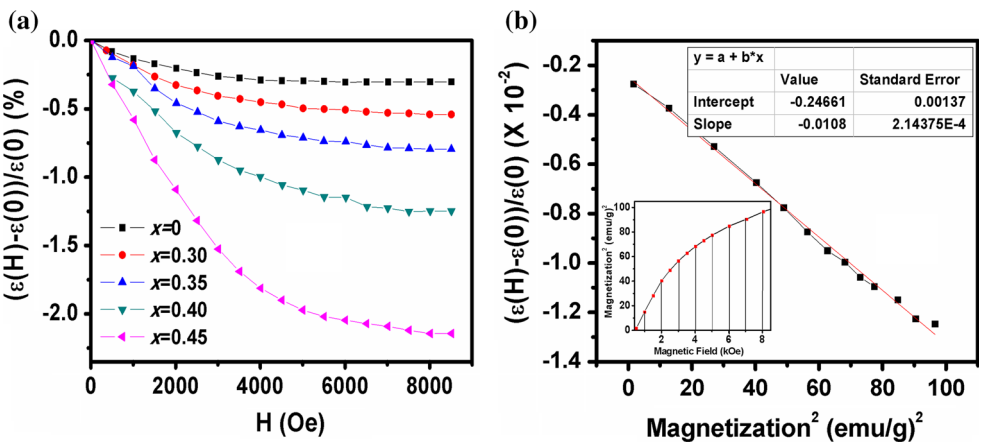

Fig. 7 **a** Magnetic field induced change in dielectric constant for $(1-x)$(0.7$BiFeO_3$–0.3$CoFe_2O_4$)–$x$$PbTiO_3$ composites. **b** Variation of magnetocapacitance with (magnetization)^2 for 0.6(0.7$BiFeO_3$–0.3$CoFe_2O_4$)–0.4$PbTiO_3$ composite, whereas the inset shows the variation of (magnetization)^2 with an applied magnetic field

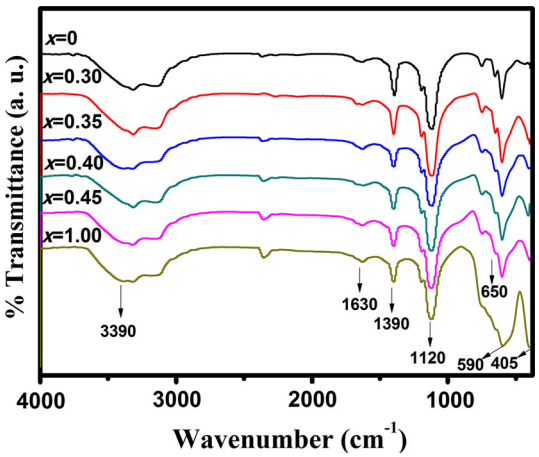

Fig. 8 FTIR spectra of $(1 - x)(0.7BiFeO_3–0.3CoFe_2O_4)–xPbTiO_3$ ceramic composites

of vibration of bismuth oxide. The band displayed around 1120 cm^{-1} in IR spectrum is ascribed to the presence of carbonate ions. The presence of band at around 1390 cm^{-1} is ascribed to the trapped nitrates. The absorption band around 1630 cm^{-1}, which exists in all the composites, is assigned to bending vibrational modes of water molecules [47]. The absorption peak lying around 3390 cm^{-1} is ascribed to the stretching vibrations of weakly bound water molecules. The presence of water in the case of composites could be due to the fact that the powder was not dry enough.

Conclusions

The three-phase composites $(1 - x)(0.7BiFeO_3–0.3CoFe_2O_4)–xPbTiO_3$ (0.7BFO–0.3CFO/PT) with $x = 0, 0.30, 0.35, 0.40, 0.45$, and 1.0 were successfully synthesized through hybrid ceramic process, where 0.7BFO–0.3CFO was prepared through sol–gel process and PT through solid-state reaction method. X-ray diffraction pattern confirms the presence of constituent phases i.e., ferrite phase (0.7BFO–0.3CFO) and ferroelectric phase (PT) of the composites. A detailed Rietveld analysis has been performed to investigate the structural changes with the inclusion of various constituents, and to ensure the presence of subsequent structural phases. TEM micrograph of 0.7BFO–0.3CFO nanoparticles reveals that the average particle size lies between 10 and 15 nm. The presence of an ordered magnetic structure is confirmed through the presence of ferromagnetic hysteresis loops at room temperature (300 K) and low temperature (5 K), as due to the presence of CFO, the spin cycloid of BFO is suppressed and locked magnetization is released. Furthermore, the temperature-dependent magnetization indicates the presence of spin glass behavior in the composites. The coupling between ferroelectric and ferromagnetic orderings is confirmed through the presence of magnetodielectric effect at room temperature. The highest value of magnetocapacitance (2.05 %) is observed for 45 mol% addition of PT content. These ceramic composites might be promising candidates as multiferroic materials. FTIR spectroscopy revealed the presence of various theoretically predicted peaks which were related to CFO, BFO, and PT phases.

Acknowledgements We would like to thank the Council of Scientific and Industrial Research (CSIR), New Delhi, India with Grant No. 03(1272)/13/EMR-II (dated 12.04.2013) for financial support.

References

1. Hu W, Chen Y, Yuan H, Li G, Qiao Y, Qin Y, Feng S (2011) Structure, magnetic, and ferroelectric properties of $Bi_{1-x}Gd_xFeO_3$ nanoparticles. J Phys Chem C 115:8869–8875
2. Eerenstein W, Mathur ND, Scott JF (2006) Multiferroic and magnetoelectric materials. Nature 442:759–765
3. Yang H, Ke Q, Si H, Chen J (2012) $0.7BiFeO_3$-$0.3BaTiO_3$-$Y_3Fe_5O_{12}$ composites with simultaneously improved electrical and magnetic properties. J Appl Phys 111:024104–024107
4. Mandal SK, Rakshit T, Ray SK, Mishra SK, Krishna PSE, Chandra A (2013) Nanostructures of Sr^{2+} doped $BiFeO_3$ multifunctional ceramics with tunable photoluminescence and magnetic properties. J Phys: Condens Matter 25:055303–055312
5. Bi L, Taussig AR, Kim HS, Wang L, Dionne GF, Bono D, Persson K, Ceder G, Ross CA (2008) Structural, magnetic, and optical properties of $BiFeO_3$ and Bi_2FeMnO_6 epitaxial thin films: an experimental and first-principles study. Phys Rev B 78: 104106–104115
6. Basu SR, Martin LW, Chu YH, Gajek M, Ramesh R, Rai RC, Xu X, Musfeldt JL (2008) Photoconductivity in $BiFeO_3$ thin films. Appl Phys Lett 92:091905–091907
7. Zhang ST, Zhang Y, Lu MH, Du CL, Chen YF, Liu ZG, Zhu YY, Ming NB, Pan XQ (2006) Substitution induced phase transition and enhanced multiferroic properties of $Bi_{1-x}La_xO_3$ ceramics. Appl Phys Lett 88:162901–162903
8. Pradhan SK, Das J, Rout PP, Mohanta VR, Das SK, Samantray S, Sahu DR, Huang JL, Verma S, Roul BK (2010) Effect of holmium substitution for the improvement of multiferroic properties of $BiFeO_3$. J Phys Chem Solids 71:1557–1564
9. Wen Z, Lv Y, Wuand D, Li A (2011) Polarization fatigue of Pr and Mn co-substituted $BiFeO_3$ thin films. Appl Phys Lett 99:012903–012905
10. Liu XH, Xu Z, Wei XY, Dai ZH, Yao X (2010) Ferroelectric, ferromagnetic, and magnetoelectric characteristics of $0.9(0.7BiFeO_3–0.3BaTiO_3)–0.1CoFe_2O_4$ ceramic composite. J Am Ceram Soc 93:2975–2977
11. Kanamadi CM, Kim JS, Yang HK, Moon BK, Choi BC, Jeong JH (2009) Synthesis and characterization of $CoFe_2O_4$–$Ba_{0.9}Sr_{0.1}TiO_3$ magnetoelectric composites with dielectric and magnetic properties. Appl Phys A 97:575–580
12. Liu XM, Fu SY, Huang CJ (2005) Synthesis and magnetic characterization of novel $CoFe_2O_4$–$BiFeO_3$ nanocomposites. Mater Sci Eng B 121:255–260
13. Mishra KK, Satya AT, Bharathi A, Sivasubramanian V, Murthy VRK, Arora AK (2011) Vibrational, magnetic, and dielectric behavior of La-substituted $BiFeO_3$-$PbTiO_3$. J Appl Phys 110:123529–123539

14. Wang N, Cheng J, Pyatakov A, Zvezdin AK, Li JF, Cross LE, Viehland D (2005) Multiferroic properties of modified $BiFeO_3$-$PbTiO_3$-based ceramics: random-field induced release of latent magnetization and polarization. Phys Rev B 72:104434–104438
15. Gheorghiu FP, Lanculescu A, Postolache P, Lupu N, Dobromir M, Luca D, Mitoseriu L (2010) Preparation and properties of (1-x)$BiFeO_3$-$x BaTiO_3$ multiferroic ceramics. J Alloys Compd. 506:862–867
16. Kumar MM, Srivinas A, Suryanarayana SV (2000) Structure property relations in $BiFeO_3$/$BaTiO_3$ solid solutions. J Appl Phys 87:855–862
17. Ma ZZ, Tian ZM, Li JQ, Wang CH, Huo SX, Duan HN, Yuan SL (2011) Enhanced polarization and magnetization in multiferroic (1-x)$BiFeO_3$-$x SrTiO_3$ solid solution. Solid State Sci 13: 2196–2200
18. Chen J, Qi Y, Shi G, Yan X, Yu S, Cheng J (2008) Diffused phase transition and multiferroic properties of $0.57(Bi_{1-x}La_x)FeO_3$-$0.43PbTiO_3$ crystalline solutions. J Appl Phys 104:064124–064128
19. Zhuang J, Chen L, Ren W, Ye ZG (2013) Synthesis, structure and dielectric properties of (1-x) [$0.9BiFeO_3$–$0.1DyFeO_3$]–$x PbTiO_3$ pseudo-binary ceramics. Ceram Int 39:S207–S211
20. Kim JS, Cheon C, Choi YN, Jang PW (2003) Ferroelectric and ferromagnetic properties of $BiFeO_3$-$PrFeO_3$-$PbTiO_3$ solid solutions. J Appl Phys 93:9263–9270
21. Yang H, Ke Q, Si H, Chen J (2012) $0.7BiFeO_3$-$0.3BaTiO_3$-$Y_3Fe_5O_{12}$ composites with simultaneously improved electrical and magnetic properties. J Appl Phys 111:024104–024107
22. Kumar L, Kumar P, Narayan A, Kar M (2013) Rietveld analysis of XRD patterns of different sizes of nanocrystalline cobalt ferrite. Int Nano Lett 3:8–19
23. Adhlakha N, Yadav KL, Singh R (2013) Implications of La and Y codoping on structural, multiferroic, magnetoelectric and optical Properties of $BiFeO_3$. Sci Adv Mater 5:947–959
24. Mazario E, Herrasti P, Morales MP, Menendez N (2012) Synthesis and characterization of $CoFe_2O_4$ ferrite nanoparticles obtained by an electrochemical method. Nanotechnology 23:355708–355713
25. Sahu N, Kar M, Panigrahi S (2010) Rietveld refinement, microstructure and electrical properties of $PbTiO_3$ ceramic materials. Arch Phys Res 1:75–87
26. Bammannavar BK, Naik LR, Chougule BK (2008) Studies on dielectric and magnetic properties of $(x)Ni_{0.2}Co_{0.8}Fe_2O_4 + (1 - x)$ barium lead zirconate titanate magnetoelectric composites. J Appl Phys 104:064123–064130
27. Fawzi AS (2011) Effect of sintering temperature on structural, electrical, magnetic hysteresis and magnetoelectric effect on $(x)Ni_{0.7}Zn_{0.3}Fe_2O_4$ + (1-x)PLZT composite by co-precipitation method. Adv Appl Sci Res 2:577–589
28. Zhang HF, Or SW, Chan HLW (2008) Multiferroic properties of $Ni_{0.5}Zn_{0.5}Fe_2O_4$-$Pb(Zr_{0.53}Ti_{0.47})O_3$ ceramic composites. J Appl Phys 104:104109–104114
29. Zhang S, Priya S, Shrout TR, Randall CA (2003) Low frequency polarization behavior of $x BiScO_3$–$y BiGaO_3$–(1-x-y)$PbTiO_3$ piezocrystals. J Appl Phys 93:2880–2883
30. Islam RA, Priya S (2008) Effect of piezoelectric grain size on magnetoelectric coefficient of $Pb(Zr_{0.52}Ti_{0.48})O_3$–$Ni_{0.8}Zn_{0.2}Fe_2O_4$ particulate composites. J Mater Sci 43:3560–3568. doi:10.1007/s10853-008-2562-9
31. Chandarak S, Ngamjarurojana A, Srilimsak S, Laoratanakul P, Rujirawat S, Yimnirum R (2011) Dielectric properties of $BaTiO_3$-modified $BiFeO_3$ ceramics. Ferroelectrics 410:75–81
32. Zhang J, Wang L, Bian L, Xu J, Chang A (2014) Structural, dielectric and piezoelectric properties of $x BiFeO_3$-(1-x)$BaTi_{0.9}$-$Zr_{0.1}O_3$ ceramics. Ceramics Int. 40:5173–5179
33. Zhang X, Sui Y, Wang X, Wang Y, Wang Z (2010) Effect of Eu substitution on the crystal structure and multiferroic properties of $BiFeO_3$. J Alloys Compd 507:157–161
34. Kambale RC, Shaikh PA, Bhosale CH, Rajpure KY, Kolekar YD (2010) Studies on magnetic, dielectric and magnetoelectric behavior of $(x)NiFe_{1.9}Mn_{0.1}O_4$ and $(1 - x)BaZr_{0.08}Ti_{0.92}O_3$ magnetoelectric composites. J. Alloys Compd. 489:310–315
35. Sone K, Sekiguchi S, Naganuma H, Miyazaki T, Nakajima T, Okamura S (2012) Magnetic properties of $CoFe_2O_4$ nanoparticles distributed in a multiferroic $BiFeO_3$ matrix. J Appl Phys 111: 124101–124105
36. Mishra KK, Satya AT, Bharathi A, Sivasubramanian V, Murthy VRK, Arora AK (2011) Vibrational, magnetic, and dielectric behavior of La-substituted $BiFeO_3$-$PbTiO_3$. J Appl Phys 110: 123529–123539
37. Gupta A, Chatterjee R (2009) Magnetic, dielectric, magnetoelectric, and microstructural studies demonstrating improved magnetoelectric sensitivity in three-phase $BaTiO_3$–$CoFe_2O_4$–poly(vinylidene-fluoride) composite. J Appl Phys 106:024110–024115
38. Kumar L, Kar M (2012) Effect of La^{3+} substitution on the structural and magnetocrystalline anisotropy of nanocrystalline cobalt ferrite ($CoFe_{2-x}La_xO_4$). Ceramic Int 38:4771–4782
39. Tang X, Dai J, Zhu X, Song W, Sun Y (2011) Magnetic annealing effects on multiferroic $BiFeO_3$/$CoFe_2O_4$ bilayered films. J Alloys Compd 509:4748–4753
40. Palkar VR, Kundaliya DC, Malik SK, Bhattacharya S (2004) Magnetoelectricity at room temperature in the $Bi_{0.9-x}Tb_xLa_{0.1}$-FeO_3 system. Phys Rev B 69:212102–212104
41. Zhou JP, Zhang YX, Lin Q, Liu P (2014) Magnetoelectric effects on ferromagnetic and ferroelectric phase transitions in multiferroic materials. Acta Mater 76:355–370
42. Kimura T, Kawamoto S, Yamada I, Azuma M, Takano M, Tokura Y (2003) Magnetocapacitance effect in multiferroic $BiMnO_3$. Phys Rev B 67:180401–180404
43. Cui Z, Sun D (2011) Adv Mater Res 533:261
44. Silva VAJ, Andrade PL, Bustamante A, Los LD, Valladares S, Mejia M, Souza LA, Cavalcanti KPS, Silva MPC, Aguiar JA (2014) Magnetic and Mössbauer studies of fucan-coated magnetite nanoparticles for application on antitumoral activity. Hyperfine Interact 224:227–238
45. Ahmad A, Bedard P, Wheat TA, Kuriakose AK, McDonald AG (1991) Surface area, XRD, and FTIR spectral characterization of chemically derived $PbTiO_3$. J Solid State Chem 93:220–227
46. Sengodan R, Chandar Shekar B, Sathish S (2012) Synthesis and characterization of $BaTiO_3$ nano particles by organic precursor method. IJMER 2:043–045
47. Bayal N, Jeevanandam P (2012) Synthesis of CuO@NiO core-shell nanoparticles by homogeneous precipitation method. J Alloys Compd 537:232–241